10th Process Technology Conference Proceedings, Toronto, Ontario, April 5-8, 1992, *Iron and Steel Society* , Warrendale, PA, 1992, pp. 291- 304.

INCLUSION PARTICLE BEHAVIOR IN A CONTINUOUS SLAB CASTING MOLD

R. C. Sussman and M. T. Burns
Armco Inc.
Research & Technology
705 Curtis Street
Middletown, Ohio 45043

X. Huang and B. G. Thomas
Department of Mechanical and Industrial Engineering
University of Illinois at Urbana-Champaign
1206 West Green Street
Urbana, Illinois 61801

ABSTRACT

The movement and entrapment of alumina inclusions in the liquid pool of a continuous slab casting machine has been investigated using a physical water model, mathematical models, and industrial experiments. The full-scale water model of the mold and sub-mold regions of a 1,930 mm wide slab caster used plastic beads with a density chosen to achieve the Stokes flotation behavior of 10-200 μm alumina inclusion particles. The mathematical model employed the finite difference method to solve the 3D Navier-Stokes and K-ε turbulence equations for the multi-phase flow behavior of the steel, argon, and inclusion particles in both the water model and continuous caster. Reasonable agreement was obtained between the calculated and observed flow patterns and inclusion flotation rates in the water model. Some differences were predicted between flow in the water and steel models. A mechanism for the entrapment of inclusions has been proposed through comparison of the model results with metallographic observations of slabs. In particular, the depth and frequency of particle entrapment below the meniscus is related to the relative depth of the particles beneath the slab surface.

INTRODUCTION

Fluid flow in the liquid pool contained by the solidifying shell in a continuous casting machine controls heat transfer, surface turbulence, and the distribution of inclusion particles. Inclusion particles may float to the top surface and become entrained into the slag layer, or they may become entrapped in the solidifying shell, where they can initiate quality problems, such as surface slivers. They are also important to internal quality of the steel, where they promote cracks and deleterious mechanical properties.

The tools available to understand the complex behavior of inclusion motion in the continuous casting mold include industrial experiments, full-scale physical water models and numerical simulations. The experiments and physical models have been very useful in the past for process design and optimization. The present work augments these tools with mathematical models, which can provide detailed insight into various phenomena which is not possible through experiments. To be effective, the mathematical models need to be verified with physical models and then combined with observations and experiments using the real steel casting machine.

The first objective of this work is to apply both physical and mathematical models to simulate fluid flow, inclusion movement and flotation within the liquid pool of a continuous slab-casting machine, including the effects of argon gas injection. In addition to providing insight into inclusion movement, the results are compared to improve and understand the potential accuracy of the mathematical predictions.

The second objective is to investigate the influence of the flow pattern on inclusion entrapment and distribution in the solidifying steel shell of a curved-mold slab casting machine. The effects of mold curvature, argon gas injection and inclusion size on flow and inclusion behavior are investigated mathematically. The results are interpreted in the light of radiographic investigations of inclusion location in the steel slabs. This work should increase our understanding of the early stages of solidification in the mold region and provide insights that will aid in the prevention of surface defects and other quality problems.

PHYSICAL WATER MODEL

Procedures

Water model experiments have been an important focus of research studies because the models allow direct observation of the liquid flow, so that simulated steel flow can be evaluated [1]. The model used in this study was constructed with the same dimensions as the mold of the continuous caster, thereby achieving both geometric and dynamic similarity between the water and steel flow as characterized by the Reynold and Froude numbers. These dimensionless numbers account for the relative influences of inertial, gravitational and viscous forces so that the internal fluid flow between the model and steel can be simulated.

The water model was built to the dimensions of the Armco Middletown Works slab caster. A steel frame supports the 25 mm thick Plexiglas plates that permit full observation of fluid flow in the mold from the meniscus to the outlet of the model and between the narrow faces. Specific dimensions of the model are listed in Table 1 and shown schematically in Figure 1. The mold is fed by a simulated tundish which maintains the water at about 1.3 m head. The water is fed through an automatic slide gate valve and the actual refractory submerged entry nozzles (SEN) used in the caster are installed on the water model.

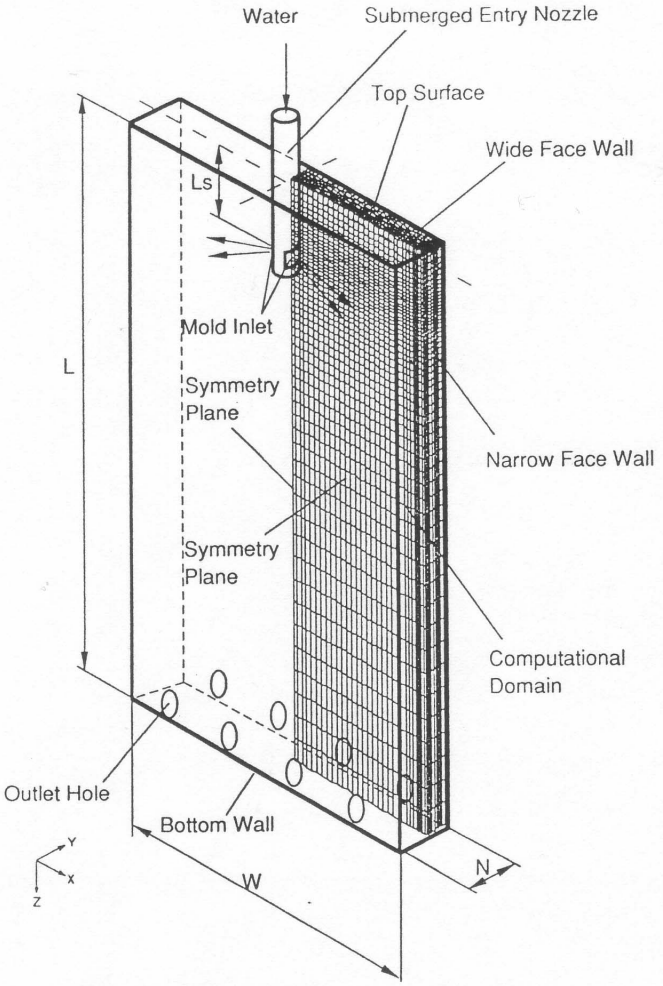

Figure 1 — Schematic physical water model and computational mesh.

An automatic level control system in the tundish using a float maintains the water at a constant level in the mold. The water is recirculated from the mold to the tundish by exiting through outlet holes shown in Figure 1 and pumped upwards.

Washable blue ink served as the dye used to visualize the flow and is neutralized by additions of chlorine tablets. The dye injection trials were used to approximate the impingement point of the flow on the narrow face of the mold. After steady-state flow conditions were attained, the dye solution was injected as a pulse into the ladle slide gate. The plastic beads used to simulate the inclusions are approximately 3.8 mm in diameter and rounded or cylindrical in shape. The effective density of the beads is about 99.5% that of water which approximately corresponds to the flotation characteristics in the water model as large 330 μm diameter alumina inclusions found in the steel slabs. The beads were added by filling an injector with a specific weight of beads and then injecting all of the beads directly into the inner tundish well at the start of the trial. Screens were constructed around the SEN just below the meniscus which entrapped all of the beads that floated into the mold flux layer. Trials were run for 10 up to 300 seconds and represent the results of at least five trials with each setup. After each trial, the beads in the screens were weighed to determine the percent of beads floated into the flux. The beads that floated out of the bottom of the mold model were also collected in a screen and weighed.

A hot wire anemometer was used to determine the velocity of the water flow in the model and assist in determining the impingement points. A special tip designed for accurate measurement in this environment was employed and the water maintained at constant temperature to stay within the calibration of the instrument. Special brackets were constructed to keep the wire tip normal to the flow direction during the measurement. Helium gas was injected into the slide gate on some trials to simulate argon injection through the submerged entry nozzle at the caster. The position of the eye of each upper and lower recirculating region or swirl was determined by observing a flag constructed with thin film attached to a wooden dowel. The eye was determined to be the position that the film was stagnant in all directions. A video camera was used to record the movement of particles and injected dyes during several of the experimental trials.

EVALUATION OF INCLUSIONS IN CAST SLABS

Inclusions in cast slabs were evaluated using a radiographic technique which provided the quantity, size distribution, and location of subsurface inclusions. The radiographs are remarkably detailed with inclusions down to approximately 0.5 mm easily identified.

A 250 mm long (casting direction) x full thickness x full width slab section was acquired for the radiographic analysis. The sample was taken from a parent low carbon (0.04%) aluminum killed slab cast under steady state operating conditions. Other than the slab width of 1727 mm, the casting conditions for the sample closely duplicated those used for both the mold water modeling and mathematical modeling results presented in Table 1.

For the radiographic analyses, slab slices were prepared from the sample according to Figure 2. The figure shows that radiographic samples were taken from three locations across the slab. The locations corresponded to the 1/4 point, centerline (1/2 point), and 3/4 point positions. At these three locations, a series of 'wafers' were cut from the sample. Each wafer, after cutting and grinding, was approximately 200 mm x 250 mm x 3.5 mm thick. Ten wafers were cut at each location corresponding to 1.3 cm intervals from the top of the slab to the centerline. In total, 30 samples were machined.

Each wafer was then X-rayed to provide a radiograph of the locations of the inclusions contained within the steel sample. The X-rays were taken for 40 seconds using a 120 kV, 10 ma. source at a standoff distance of 1.49 m.

TABLE 1

CONDITIONS FOR EXPERIMENTAL AND NUMERICAL RUNS

	Water Model	Steel Caster
Model Length L (m)	2.152	3
Model Width W (m)	1.93	1.93
Model Thickness N (m)	0.238	0.238
SEN Port Diameter (mm)	51 (for experiment)	51
SEN Port Width (mm)	51 (for prediction)	51
SEN Port Height (mm)	66 (for prediction)	66
Nozzle Angle (°)	25° down	--
Jet Angle (°)	25° Down	25° down
Submerged Depth L_n (m)	0.15	0.15
Casting Speed (mm/s)	15.2	15.2
Density of Liquid (kg/m^3)	1000	7020
Laminar Viscosity (Pa/m^2)	0.001	0.0055
Inlet Velocity (m/s)	1.156	1.156
Inlet Velocity v_x (m/s)	1.048	1.048
Inlet Velocity v_z (m/x)	0.489	0.489
Inlet K (m^2/s^2)	0.0502	0.0502
Inlet ε (m^2/s^3)	0.457	0.457
Gas	Helium	Argon
Gas Vol. Frac. at SEN Inlet (%)	3.3	3.3
Gas Vol. Frac. at Modl Inlet (%)	2.8	11
Gas Material Density (kg/m^3)	1.6	0.18
Gas Mass Flow Rate (m^3/s)	0.000236	0.000236
Gas Temp. at SEN Inlet (°C)	25	25
Gas Temp. at Mold Inlet (°C)	25	1550
Bubble Size at SEN Inlet (mm)	5	3
Bubble Terminal Velo. (m/s)	0.024	0.024
Inclusion Particle Size (μm)	2500	170, 100 and 20
Particle Material Density (kg/m^3)	998	2700
Mold Inner Radius (m)	--	10.5
Mold Outside Radius (m)	--	10.72

Results and Discussion

The observed inclusions were divided into three categories by size, 0.13-0.25 mm, 0.25-0.64 mm, and >0.64 mm. Inclusion size was estimated using corresponding penetrameter radiographs printed on each X-ray. Figure 3 presents a total count of the inclusions observed on the radiographs from all 30 wafers. The figure indicates that 60% of the inclusions were observed in the smallest size category. The middle category contained 30%, and the largest category contained 10%. The observed size distribution suggested the radiographs were identifying what would be the right hand tail of a normal inclusion particle size distribution.

More detailed results are presented in Figure 4. This figure presents two graphs. Figure 4a is the inclusion count observed for each wafer from the top surface at the inside radius to the slab center at the centerline of the slab. The slab centerline position would correspond to the location of the SEN. Figure 4b shows similar data for an average of the 1/4 and 3/4 width positions.

A comparison between the two indicates a remarkable difference in the frequency, size distribution, and depth of defects between these two locations. The centerline samples displayed only a few inclusions in the smaller sizes. However, the 1/4 and 3/4 width positions displayed significantly more inclusions in all three size categories. The inclusions also tend to be deeper in the slab.

The observed difference in inclusion location between the centerline and the quarter point positions has been suggested qualitatively from mold water model. These studies have indicated that the strong exit flow from the SEN tends to carry inclusions outward away from the centerline. These inclusions were presumed to be more apt to be caught toward the outside edges of the slab. The radiographic results tend to support that belief.

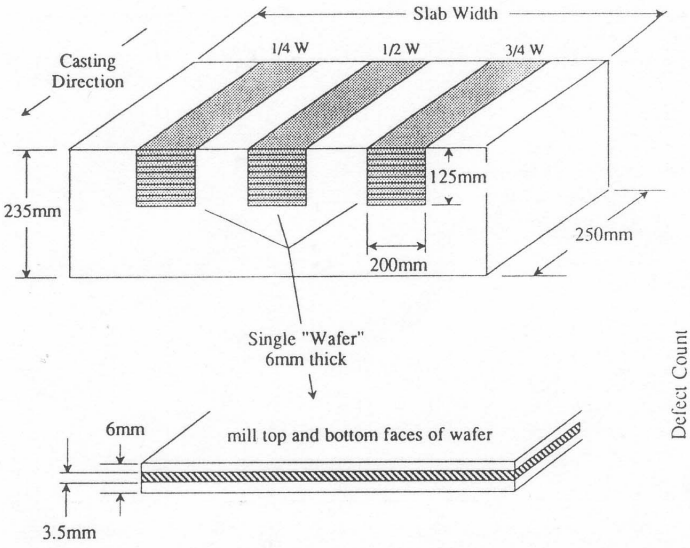

Figure 2 — Sample positions for radiographic analysis

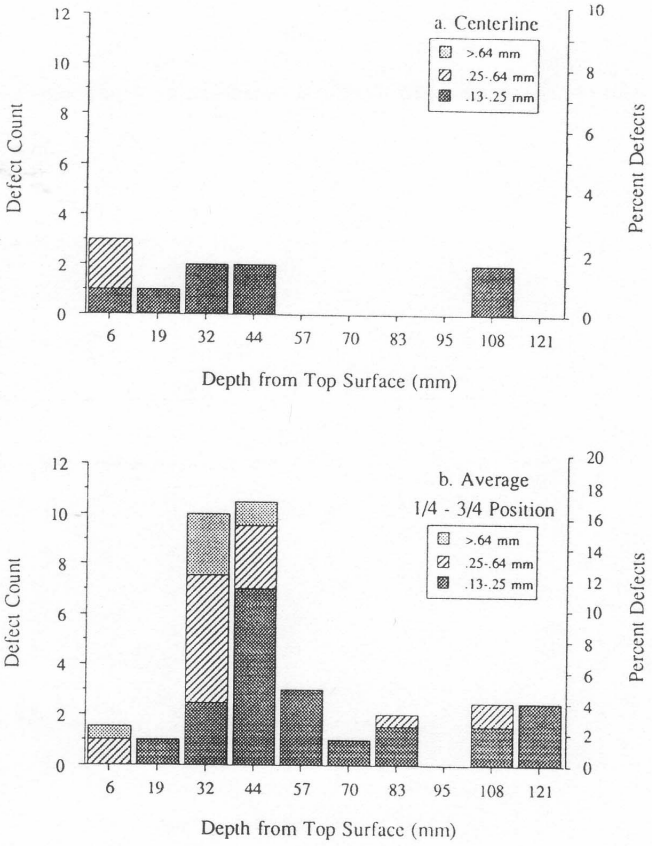

Figure 4 — Edge vs. centerline defect distribution from slab evaluation

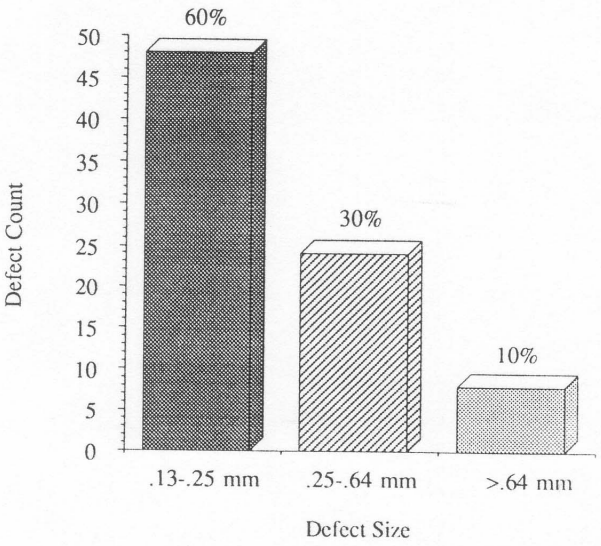

Figure 3 — Size distribution of inclusions in slab evaluation

MATHEMATICAL MODEL DESCRIPTION

To predict fluid flow in continuous slab casting, a mathematical model was employed to calculate fluid flow velocities within the molten steel pool of a slab casting machine, fed by a bifurcated, submerged entry nozzle. Figure 1 shows the model domain used to simulate flow inside the water model. Owing to the regular rectangular geometry, a computer program based on finite difference calculations, MUPFAHT[2], was chosen for this complex problem. The model solves the Navier-Stokes equations in three dimensions using the popular K-ε two-equation turbulence model to simulate the turbulent, recirculating flow involved in the present problem. The governing equations for conservation of mass, momentum, turbulent kinetic energy and dissipation can be found in Appendix I.

Boundary Conditions

Inlet boundary conditions to the model, including angle of the jet, its velocity profile, turbulence and kinetic energy levels, are based on a separate three-dimensional finite element model of the nozzle, described elsewhere[3,4]. To simplify the geometry of the inlet plane in the present mold model, the circular nozzle port was treated as an equivalent area rectangle, chosen to match the outlet jet speed. Only

one quarter of the mold was modeled and the vertical symmetry planes were imposed by setting the normal velocity and shear stresses to zero. The top surface employed this same boundary condition.

Standard wall law function approximations were employed to calculate tangential velocity, K, and ε, in the laminar boundary layer between the first node and the solid interior walls[5,6]. When simulating the steel caster, only the liquid pool was modeled, so the computational difficulties associated with modeling solidification were avoided. To account for the dendritic surface of the solid/liquid interface forming the boundary of the model domain in this case, the roughness factor used in the wall laws for liquid steel was decreased from 8.8 to 0.8[7] .

Flow exits the bottom of the physical water model through four pipes located at the bottom of the wide face, to allow removal of water at a volume flow rate corresponding to the casting speed. To account for this, the bottom plate is modeled numerically as a solid wall, with the holes created near the bottom of the wide face wall by fixing the outlet velocity. The value was chosen to produce the volumetric flow rate corresponding to the given casting speed and to achieve a mass balance with the inlet. For the steel caster, the simple fully developed flow conditions of zero normal gradients act along the bottom boundary of the model domain.

Gas Injection

The injection of argon gas bubbles changes both the flow pattern and the behavior of inclusions, affecting both their residence time and entrapped locations in the steel shell. The argon gas bubbles in liquid steel and helium bubbles in the water present a similar numerical challenge to the simulation methods for two-phase flow. To simplify the problem, the gas bubbles are assumed to be spheres with a uniform size. Their terminal rising velocity, v_{tb}, is calculated immediately after entering the domain, according to size using an experimental correlation[8]. The drag force acting on the bubbles is balanced by the buoyancy force. From these assumptions, an extra force acting on liquid due to motion of the gas bubbles is obtained as following:

$$f_b = \sigma_b g(\rho_l - \rho_b) \approx \sigma_b g \rho_L$$

To calculate the motion of the bubbles themselves, it is assumed that the bubbles disperse like a species in gas-liquid mixture due to turbulent transport. This bubble diffusion is thus expressed as:

$$\nabla \bullet (\rho_l v_b \nabla \sigma_b) = \nabla \bullet (D_t \nabla \sigma_b)$$
$$v_b = v_1 - v_{tb}$$

A zero-gradient condition for gas bubble volume fraction is set for all boundaries except the inlet of the domain. This condition is consistent with no mass flow through the walls while it allows bubbles to leave both the top surface and bottom of the domain.

Inclusion Particles

To understand the behavior of inclusions arriving in the incoming jet of liquid steel, trajectories of individual inclusion particles were tracked through each simulated flow field. To do this, several assumptions were made:

1) the inclusion particles have uniform size;
2) only drag and buoyancy forces act on each particle;
3) the volume fraction of particles is so small that they have no influence on motion of the liquid, bubbles, or other particles;
4) the particles are small enough to achieve their local terminal velocity wherever they move.

5) Particle trajectories can then be obtained from:

$$\frac{dr_p}{dt} = v_p$$

Integrating this equation numerically gives the displacement vector $\mathbf{r}=\mathbf{r}(t)$ which represents the particle location at any time. The particle velocity, v_p, is found from its terminal velocity relative to the mixture of liquid and gas, v_{tp}:

$$v_p = v_{mix} - v_{tp}$$

where: $$v_{tp} = \frac{g(\rho_l - \rho_p)dp^2}{18\mu_1} \quad \frac{1}{(1+\frac{1}{6}\mathrm{Re}^{0.687})}$$

$$\mathrm{Re} = \frac{\rho_l |v_p - v_{mix}| dp}{\mu_1}$$

To derive the above expressions, a modified form of the Stokes' drag force is used which includes the influence of turbulence and non-spherical particle shape[8-9]. The effect of the gas bubbles on the inclusion movement is also taken into account by basing the equations on the mixture velocity, density and viscosity of the multi-phase system which are defined as:

$$v_{mix} = (1 - \sigma_b)\, v_1 + \sigma_b\, v_b \approx v_1 - \sigma_b\, v_{tb}$$
$$\rho_{mix} = (1 - \sigma_b)\, \rho_1 + \sigma_b\, \rho_b \approx \rho_1$$
$$\mu_{mix} = (1 - \sigma_b)\, \mu_1 + \sigma_b\, \mu_b \approx \mu_1$$

Curvature of the mold has an important influence on the motion of inclusion particles, since their buoyancy may cause them to become entrapped against the upper inside radius shell before they can float or be carried to the top surf ace of the mold. This effect was incorporated into the present straight-mold model simply by varying the direction of gravity as a function of distance down the mold.

$$g_z = |g| \cos(z/R)$$
$$g_x = -|g| \sin(z/R)$$

Thirty-six different particles were introduced into the numerical domain at different positions in the inlet plane to simulate the diverse possible paths that particles may take through the water model or caster. Each trajectory was tracked until the particle either floated across the top surface, was entrapped by a mathematical screen (water model), exited the bottom of the domain, or touched a wall. In steel caster simulations, particles were assumed to be trapped by the growing shell or top surface at the location where they first touch a domain boundary. This produced a residence time and final trapped location for each particle, provided the time limit of 300s was not exceeded.

Solution Procedure

Finite difference equations were obtained from the governing partial differential equations (Appendix I) by applying a seven-point hybrid scheme to each control volume or cell. The resulting algebraic equations were solved by ASDF using the SIMPLE algorithm[11], which involves a semi-implicit ADI iteration algorithm with a pressure-velocity modification. A staggered grid of nodes and careful source-linearized procedures was adopted to achieve stable convergence while limiting false numerical diffusion. The current solution method employs successive substitution using an under-relaxation factor of 0.2 or 0.3, until the maximum relative residual error and maximum relative error between successive solutions fall below 0.1%. This typically requires about 3000 iterations. The post processor FIPOST of the commercial finite element program FIDAP was then used to visualize the results, plot velocities, and track the trajectories of the inclusion particles. The standard mesh, shown in Figure 1, consists of a 16 by 34 by 60 grid of nodes. The input conditions for model runs are listed in Table 1.

RESULTS

Physical and Mathematical Models

The results predicted by the mathematical model and the experimental measurements using the water model are compared in Figures 5 through 8 and Tables 2 and 3. Figure 5 illustrates the three-dimensional flow pattern viewed from different directions. There are two large recirculating zones in the upper and lower parts of the model, similar to the flow pattern observed in the water model, both with and without gas injection. Because the bifurcated nozzle sends flow into the plane of a relatively thin cavity, the resulting flow pattern is relatively uniform through the thickness of the mold over most of the mold interior. There is little recirculating except near the inlet and jet impingement point. The velocity component in the horizontal planes through the mold thickness is quite small everywhere except very near the outlet holes. Thus, flow in the mold can be characterized by the location of the "lower eye," "upper eye," and "impingement point." These terms are explained in Figure 6 and Table 2 compares the predicted and measured values.

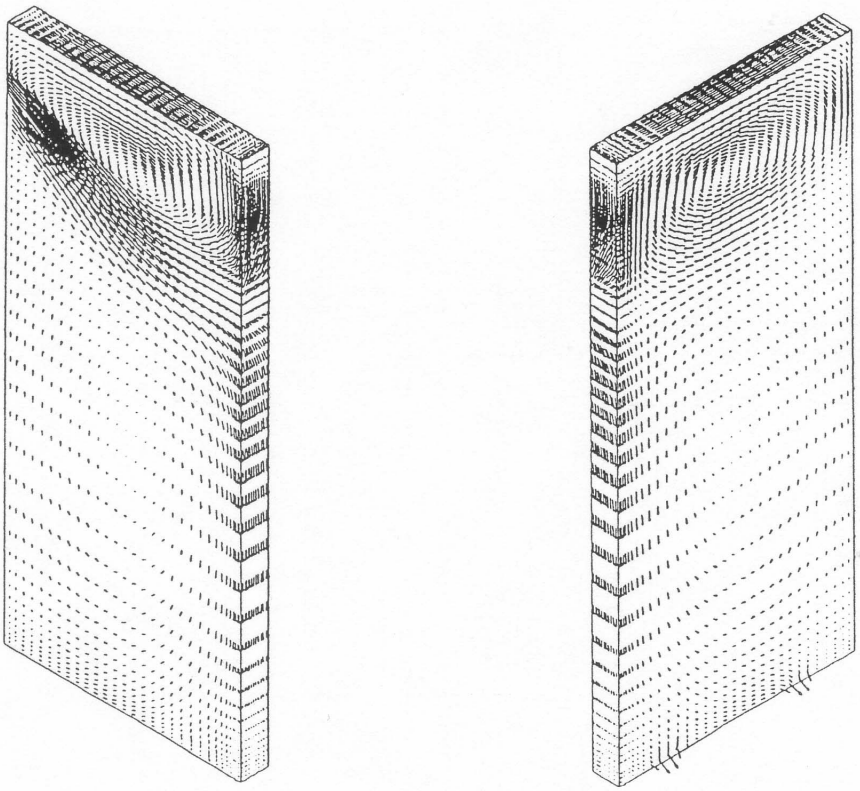

(a) Viewed Toward the Center Plane (b) Viewed Toward the Wall

Figure 5 — Velocity vectors viewed from different directions from mathematical model.

TABLE 2

EXPERIMENTAL AND PREDICTED EYES AND IMPINGEMENT POINT IN WATER MODEL

	Water Model No Gas		Water Model With Gas		Steel Caster No Gas	Steel Caster With Gas
	Pred.	**Exp.**	**Pred.**	**Exp.**	**Pred.**	**Pred.**
Lower Eye						
Dist. to CL (m)	0.521	0.546	0.521	0.533	0.465	0.483
Depth (m)	1.143	0.794	1.041	0.762	1.492	0.907
Upper Eye						
Dist. to CL (m)	0.521	0.552	0.579	0.533	0.483	0.599
Depth (m)	0.254	0.203	0.198	0.235	0.311	0.082
Impingement Point Depth (m)	0.498	0.495	0.442	0.483	0.569	0.333

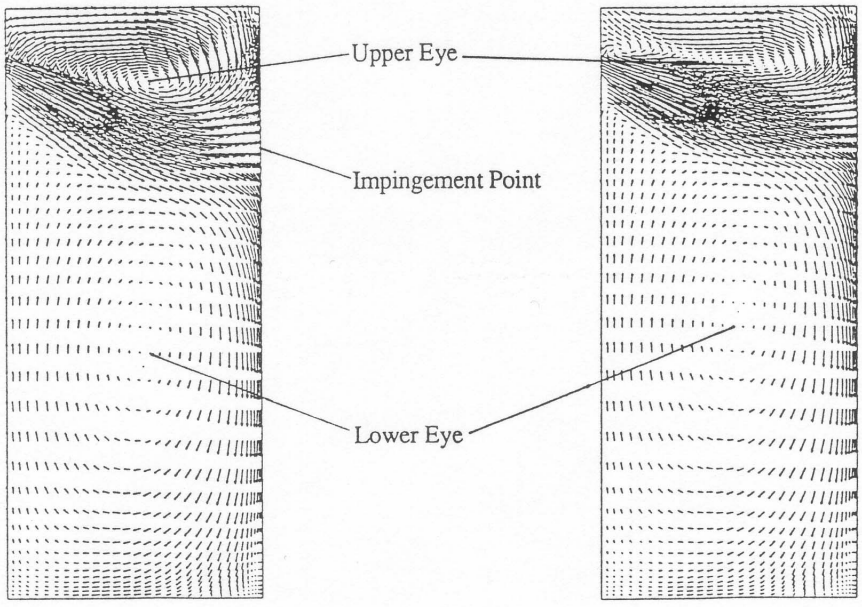

(a). No gas.

(b). With gas.

Figure 6 — Velocity vectors viewed toward the center plane from mathematical model.

There are three primary modes of inclusion movement. At a short distance after the water exits the outlet port the flow splits into an upward flow, into the upper swirl and a downward flow, which leads to the lower swirl. The inclusions which flow upwards normally migrate rapidly into the flux layer after possibly circulating within the upper eye for a brief time. The inclusions which follow the downward flow will often circulate back around the lower eye, migrate back into the upper eye, and then get removed into the flux layer. The inclusions of greatest concern are those that get caught in the lower eye and continue to circulate within this region. These inclusions can get caught in the advancing shell within the lower eye or, more dangerously, drop below the lower swirl past the critical curvature point on the curved mold caster and then become entrapped in the solidifying shell.

Helium gas bubble injection is very influential on the flow pattern and the inclusion movements. Both the mathematical and water model results demonstrate that the buoyancy of the gas bubbles shifts the recirculating patterns upward, as indicated by the results in Table 2. This effect is not seen as clearly in the experiments as in the predictions, since gas flow also increases turbulent eddy motion, which moves the eye locations around with time. However, it appears that the mathematical model slightly overestimates the effects of gas bubbles on liquid flow. This discrepancy likely reflects the inability of the model to allow the bubbles to move independently to the liquid.

Typical inclusion particle trajectories are shown in Figure 7, where the "screen" denotes the location of a physical screen placed in the water model to trap inclusions. A numerical screen located at the same position in the model domain served the same purpose by determining the "flotation time" for each particle crossing this plane from above. Three kinds of typical particle trajectories without gas are seen in this figure. In Figure 7(a), the particle travels with the fluid jet toward the impingement point, moves into the upper swirl and is captured by the screen after only 13 seconds. In Figure 7(b), the particle moves downward for one rotation through the low swirl, resulting in a longer floatation time of 55 seconds. The particle in Figure 7(c) remained trapped in the lower swirl over 130 seconds.

The predicted and measured inclusion particle flotation times are presented in Table 3. Despite the small sample size of only 36 particles used in the simulations, there is reasonable agreement between the predictions and water model measurements. In both models, the majority of the particles are removed at the top surface within 100 sec. A large portion of these float out in less than 10 sec. The only significant discrepancy is that particles took more time to float out in the experiments, particularly when no gas was present. This might imply that drag forces on the randomly shaped particles are even greater than mathematically modeled. Model predictions were found to be sensitive to the drag force.

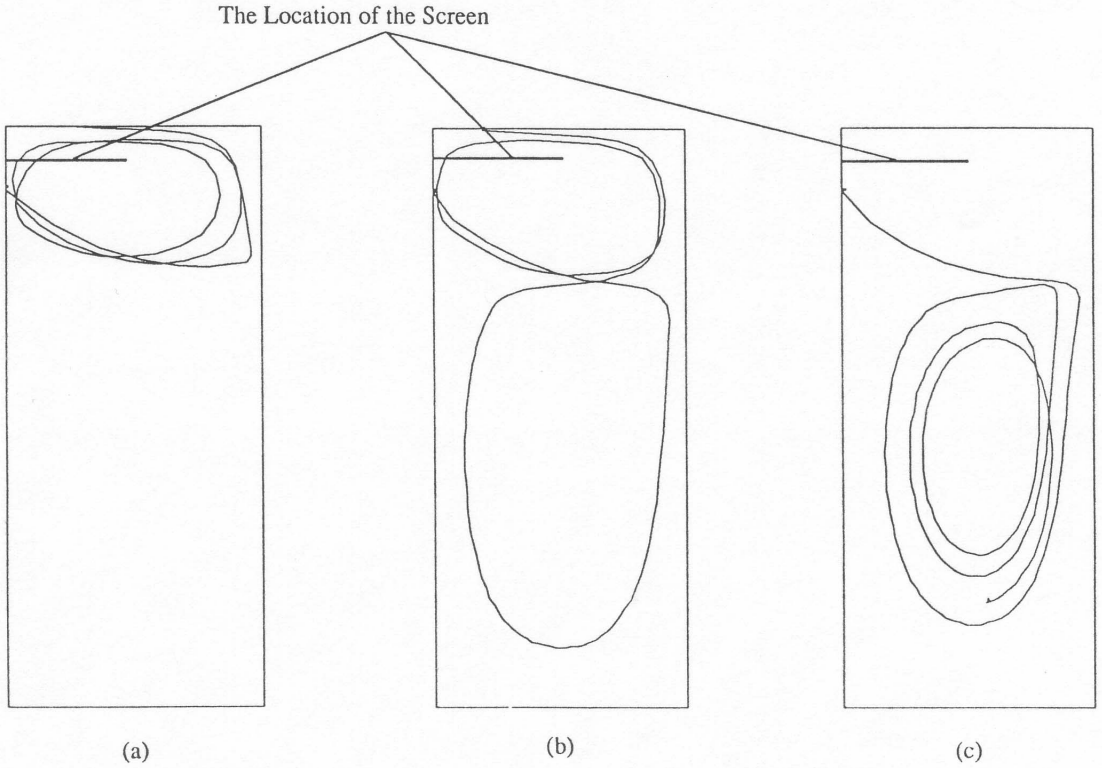

Figure 7 — Predictions of mathematical model of typical particle trajectories in water model.

TABLE 3

PROBABILITY OF FLOTATION TIME IN WATER MODEL

	No Gas		With Gas	
Flotation Time (s)	Prediction	Experiment	Prediction	Experiment
<10	42%	22.3%	47%	45.5%
10-100	28%	27.6%	25%	37.6%
100-300	0	27.6%	0	9.6%
>300	2%	0.2%	11%	0.2%
Below Model Depth	28%	22.3%	17%	7.1%
Total	100%	100%	100%	100%

Since the side walls cannot trap particles, only those that leave the mold bottom never float. This accounted for about a fourth of the particles with no gas but less than 10% when gas was injected. The mathematical model slightly overpredicts the particle fraction that never floats. Since the model tracked particle paths for only 300 sec., a few particles were still circulating after that time, both mathematically and physically.

Gas bubble injection is seen to enhance flotation of the inclusions in both the mathematical and physical models. The magnitude of the effect is seen to be more significant in the physical model than in the calculations. This indicates that bubble-particle interactions were enhanced beyond that accounted for in the model. One possible reason for this is the occasional attachment of inclusion particles to the gas bubbles. It is suspected that the same mechanism may occur in the steel caster, which would explain one of the benefits of argon use.

Steel Slab and Mathematical Model

The model was next used to predict flow and inclusion entrapment in the steel caster. Differences in the model include the use of a bottomless domain, changing gravity to account for curvature, and substituting steel, argon, and alumina properties for the fluid, gas, and particles.

Measurements of inclusion depths in the slab were compared with results from a solidification model, CONID, to find the approximate distance down the caster corresponding to where the inclusions were entrapped.[12,13,14] The results are presented and compared with the predicted location of inclusions in Table 5. Distances below the meniscus are reported as ranges, corresponding to the range of depths where inclusions were found.

The predicted flow pattern in the steel caster is very similar to that in the water model, despite the differences. Many of the inclusion particle paths are similar to those found in the water model, as seen in Figure 8. However, curvature of the mold has an important influence on the paths taken by inclusions deep in the caster. Figure 8 shows that inclusions that enter the lower recirculating zone actually spiral around with the liquid while simultaneously drifting slowly toward the inside radius. Particles can become entrapped at any location during their spiral, if they touch a wall. But, entrapment is most likely where the fluid is moving slowly and the component of the buoyancy force directed towards a wall is largest. This corresponds to the larger inclusions near the inner radius broad face surface, especially at the point of deepest penetration beneath the liquid surface.

The experimental and numerical results of the inclusion studies in a steel caster are also shown in Table 4 and Table 5. These results are in good general agreement. The large particles are measured to be trapped at the average depth of 1.51 m down the caster for the 1/4 lines, while the predicted entrapment depth is 1.98 m for those particles trapped in the same region (within 10 cm of the quarter line across the width).

For the observed recirculation patterns, the point of deepest penetration roughly corresponds to the 1/4 line across the wide face. Both experiments and calculations find that more entrapment occurs here, as expected. Tables 4 and 5 show that the average predicted entrapment depth of 100 μm particles across the entire width, only 1.84 m, is less than the 1.98 m depth for the 1/4 line particles. It should be noted that both these depths are underestimated, since they do not include 4 particles that moved deeper than 3 m. However, these predictions agree with experimental findings that average entrapment depth is always greater beneath the 1/4 line (Table 5).

Near the center line, particle entrapment positions are shallower and the chances of entrapment are smaller. No large particles were found entrapped within 100 mm of the centerline in either the experiments or model studies. This is understandable, since the slow flow and progressively decreasing buoyancy forces in this region together allow particles moving up near the centerline to float out of the region without being entrapped.

TABLE 4

INCLUSION FLOTATION TIME AND
CALCULATED ENTRAPMENT POSITIONS IN STEEL CASTER

	Percentage of Inclusion Particles				
	No Gas No Curvature	No Gas With Curvature	With Gas With Curvature		
Inclusion Diameter	**d_D = 100 μm**	**d_D = 100 μm**	**d_D = 170 μm**	**d_D = 100 μm**	**d_D = 20 μm**
Flotation Time					
10 s	30.6%	30.6%	38.8%	27.8%	11.1%
10-100 s	8.3%	44.4%	55.6%	52.8%	13.9%
>100 s	61.1%	25.0%	5.6%	19.4%	75.0%
Total	100%	100%	100%	100%	100%
Entrapped Positions					
Top	27.8%	30.6%	44.4%	38.8%	11.1%
Wide Face	0%	27.8%	33.3%	27.8%	5.6%
Narrow Face	16.7%	6.7%	22.3%	16.7%	11.1%
Below 3 m	30.5%	8.3%	0%	11.1%	55.6%
After 300 s	25.0%	16.6%	0%	5.6%	16.7%
Total	100%	100%	100%	100%	100%
Avg. entrap. depth	--	--	1.80 m	1.84 m*	>3 m

This is the minimum average value ignoring particles below 3 m.

From Table 4 and Table 5, inclusion size is seen to have a tremendous effect on their flotation behavior in steel. Larger inclusions are predicted to float out to the top slag layer faster and in greater numbers. Consequently, the percentage of particles removed from the top surface of the steel increases from 11.1% to 38.8% to 44.4% for particle size ranging from 20 to 100 to 170 μm (Table 4). Both experiments and modeling results show that particles with smaller diameters are much more likely to go to deeper part of the caster. Table 4 predicts that the number of particles penetrating deeper than 3 m increases from 0% to 11.1% to 55.6% as particle size decreases from 170 to 100 to 20 μm. This compares with a similar increase in measured inclusions at the 1/4 lines entrapped deeper than 3 m increasing from 0% to 15% to 47% for inclusion size decreasing from >64 to <25 μm, as shown in Table 5.

Small particles also have longer residence time (flotation time) in the mold, since they travel with the fluid more readily. The smaller the particles, the larger their average entrapment depth down the caster and the smaller their fraction floating to the top layer. Table 4 shows that after 300 seconds of travel with gas injection and curvature present, 17% of the 20 μm numerical particles continue to circulate in the mold. This fraction decreases to 5.6% and 0% for 100 μm and 170 μm particles respectively.

Curvature of the mold greatly increases the probability of inclusions becoming entrapped on the inner-radius wide face. Table 4 predicts that more than one quarter of the large particles (>=100 μm) become entrapped against the inner-radius wide face, both with and without gas injection, while none are trapped without curvature. The fraction of inclusions trapped by the wide face decreases with decreasing particle size. Curving the mold decreases the chances of particles moving deep into the caster, since they become trapped against the inner radius wide face instead.

Injecting argon gas with the liquid steel is predicted to enhance the flotation of inclusions. This agrees qualitatively with the experimental findings in Table 4, showing that the argon gas shortens the residence time of particles and increases the fraction floating to the top surface. The change in flow pattern due to the argon gas

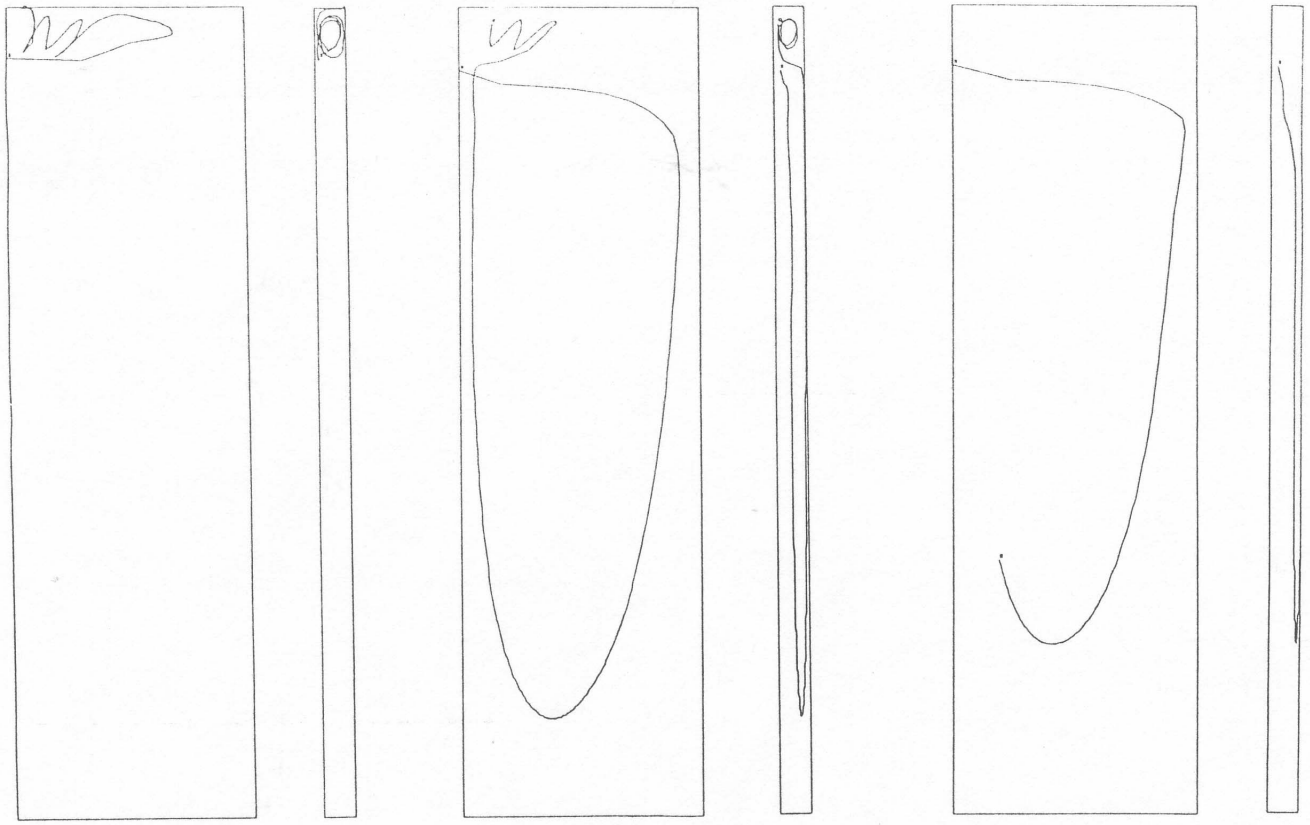

Figure 8 — Predictions of mathematical model of inclusion trajectories in curved steel caster.

TABLE 5

DISTRIBUTION OF INCLUSION ENTRAPMENT POSITION
(BENEATH MENISCUS)

		Percentage of Inclusion Particles							
		Large (d_D > 640μm)				Medium (250μm <d_D <640μm)		Small (130μm <d_D <250μm)	
Distance Below Surface (m)	Distance Below Meniscus (m)	1/4 Lines		Center Line		1/4 Lines	Center Line	1/4 Lines	Center Line
		Pred.	Exp.	Pred.	Exp.	Exp.	Exp.	Exp.	Exp.
0.25	0-.25	0	13%	0	0	10%	100%	0	12%
0.25	.25-1.0	0	0	0	0	0	0	5%	13%
1.0	1.0-2.0	50%	62%	0	0	50%	0	13%	25%
2.0	2.0-3.0	50%	25%	0	0	25%	0	35%	25%
>2.25	>3.0	--	0	0	0	15%	0	47%	25%
Averaged Entrapment Depth (m)		1.98*	1.51	N.A.	N.A.	3.36	0.05	6.39	4.97

*This value is based on the four 100 μm particles entrapped within 10 cm width of 1/4 line.

appears to encourage inclusions to be trapped against the narrow face. It should be noted that the effect of argon is predicted to be relatively small, and some of the calculated differences might be due to the small total number of inclusions (36) considered. For example, the fraction of particles going down below 3 m increases from 8.3% (3 numerical particles) without argon to 11.1% (4 numerical particles) with argon. The mathematical model does not simulate the possible flotation mechanism of inclusions attaching to gas bubbles.

Inclusions are predicted to become entrapped anywhere during their spiral path. However, entrapment is most likely at the point of deepest penetration beneath the liquid surface. This is because the component of buoyancy forces towards the inner radius increases with distance below meniscus. Large inclusion clusters are likely to be introduced into the caster during sudden events, such as by dislodging a partial clog in the SEN. To avoid potentially severe defects, it is very important that these inclusion clusters float into the protective slag layer. This becomes unlikely if the particles travel into the lower recirculating zone.

The water model and mathematical model results for the steel caster are in reasonable agreement for the flotation times of larger inclusions with or without gas injection, by comparing the results from Tables 3 and 4. The results suggest that the water model is a useful tool for inclusion movement silimitude for steel caster molds.

CONCLUSIONS

1. Difficult problems such as understanding inclusion motion in steel are best tackled using industrial experiments, physical models and mathematical models. The insights derived from these three tools together surpass the individual results.

2. Mathematical models are reasonably able to reproduce results of fluid and inclusion movement in the mold region of a continuous casting machine.

3. Inclusion motion is greatly affected by particle size for the casting conditions used in this study. Large inclusions are likely to become entrapped just below the mold by following a spiral path while traveling with the liquid in the lower recirculating zone and simultaneously floating toward the inner radius shell of the wide face. Few large inclusions travel deeper than 3 m below the meniscus, while the majority of smaller inclusions are trapped deep in the caster. More than one third of large inclusions float out to the top surface, while small inclusions are much less likely to do so.

4. Mold curvature makes inclusion entrapment by the shell on the inner-radius of the wide face easier, consequently making their flotation to the top slag layer less likely.

5. Argon gas injection enhances the flotation of inclusions and so appears to be beneficial in their removal. The mathematical model may under-predict this effect.

6. Inclusions are more likely to become entrapped in the shell when the flow pattern takes them deeper below the meniscus, where buoyancy forces due to curvature are greater. This especially occurs at the 1/4 mold width positions.

ACKNOWLEDGEMENTS

The authors wish to thank the steel companies: Armco Inc. (Middletown, OH), Inland Steel Corp. (East Chicago, IN), LTV Steel (Cleveland, OH) and BHP Co. Ltd. (Wallsend, Australia), for grants which made this research possible and for the provision of data. This work is also supported by the National Science Foundation under grant #MSS-8957195. Thanks are also due to Don Hershey, for work on the nozzle, Fluid Dynamics Inc. (Evanston, IL) for help with the FIDAP program and the National Center for Supercomputer Applications at the University of Illinois for time on the Cray-XMP/48 and Cray 2 supercomputers.

NOMENCLATURE

d_p	inclusion particle size
D_t	turbulent diffusivity of liquid
f_b	force vector acting on liquid due to gas bubbles
f_{bi}	i component of f_b
f_i	body force component in i direction
$\mathbf{g}$	gravitational acceleration vector
K	turbulent kinetic energy
p	pressure
R	Caster inner radius (m)
Re	Reynolds number of relative motion between inclusions and gas-liquid mixture
r_p	displacement vector of inclusion particles
$\mathbf{v}$	velocity vector
v_i	liquid velocity component in i direction
v_{mix}	effective velocity vector of the gas-liquid mixture
v_m	liquid velocity component parallel to the wall
v_n	liquid velocity component normal to the wall
v_t	terminal velocity vector
v_{tb}	terminal velocity vector of gas bubbles
v_{tp}	terminal velocity vector of inclusion particles
z	distance below meniscus (top surface)
ε	dissipation rate of turbulent kinetic energy
μ	liquid laminar viscosity
μ_t	liquid turbulent viscosity
ρ	material density
σb	gas bubble volume fraction
τw	shear stress at the wall

Subscripts

b	gas bubble phase
l	liquid phase
i	i direction (x, y, or z)
j	j direction (x, y, or z)
,i	$\partial/\partial x_i$
ij	repeated indicies imply summation
mix	gas-liquid-particle mixture
p	inclusion particles

REFERENCES

1. J. Herbertson, Q. L. He, P. J. Flint, R. B. Mahapatra, "Modelling of Metal Delivery to Continuous Casting Molds," 1991 Steelmaking Conference Proceedings, pp. 171-185.

2. X. Huang, "Studies on Turbulent Gas-Particle Jets and 3-D Turbulent Recirculating Gas-Particle Flows," Ph.D. Thesis, Tsinghua University (China), 1988.

3. B. G. Thomas, L. M. Mika, "Simulation of Fluid Flow and Heat Transfer Inside a Continuous Slab Casting Machine," Metallurgical Transactions, Vol. 21B, 1990, pp. 387-400.

4. D. E. Hershey, B. G. Thomas, "Turbulent Flow of Steel through Submerged Bifurcated Nozzles in the Continuous Casting Process," in Second International Conference on Application of Mathematical and Physical Models in the Iron and Steel Industry, Toronto, 1992.

5. B. E. Launder, D. B. Spalding, "The Numerical Computation of Turbulent Flows," Computer Methods in Applied Mechanics and Engineering, Vol. 3, 1974, pp. 269-289.

6. B. G. Thomas and F. M. Najjar, "Finite-Element Modeling of Turbulent Fluid Flow and Heat Transfer in Continuous Casting," Applied Mathematical Modeling, Vol. 15, April 1991, pp.226-243.

7. F. M. Najjar, "Finite-Element Modeling of Turbulent Fluid Flow and Heat Transfer through Bifurcated Nozzles in Continuous Steel Slab Casters," M.S. Thesis, University of Illinois at Urbana-Champaign, 1990.

8. S. L. Soo, Fluid Dynamics of Multi-phase System, Blaisdell Publishing Co., Waltham, MA, 1967.

9. L. Zhou, X. Huang, "Predictions of Confined Turbulent Gas-Particle Jets by an Energy Equation Model of Particle Turbulence." Science in China (Series A), Vol. (12), 1988, pp. 1262-1268.

10. S. L. Lee, "Particle Drag in a Dilute Turbulent Two-Phase Suspension Flow," J. Multiphase Flow, Vol. 13(2), 1987, pp. 247.

11. S. V. Patankar, Numerical Heat Transfer and Fluid Flow. McGraw-Hill, 1980.

12. B. G. Thomas, F. M. Najjar, and L. J. Mika, "The Removal of Superheat from Continuous Casting Molds," Proc. F. Weinberg Int. Symposium on Solidification Processing, 29th Canadian Inst. Min. Met. Conf.. Hamilton, Ontario, J. E. Lait and I. V. Samarasekera, eds., Pergamon Presss, Inc., Toronto, 1990, pp. 131-145.

13. Thomas, B. G., and B. Ho, "Heat Conduction and Solidification Model of Continuous Casting Using a PC-Based Spread Sheet Program," Materials Processing in the Computer Age, edited by V. R. Voller, M. S. Stachowicz, and B. G. Thomas, Proceedings of the International Symposium on Materials Processing in the Computer Age, Feb. 17-21, New Orleans, LA, Feb. 1991, The Minerals, Metals, and Materials Society, Warrendale, PA, 1991 pp. 293-305.

14. Bryant Ho, "Characterization of Interfacial Heat Transfer in the Continuous Slab Casting Process," Masters Thesis, University of Illinois, Urbana, IL, 1992.

APPENDIX I

Governing Equations

The six governing equations for 3-D, incompressible flow with the K-ε turbulence model are as follows:

$$v_{j,j} = 0 \qquad \text{(A-1)}$$

$$\rho\, v_j v_{i,j} = -p_{,i} + \rho\, f_i + [\,\mu_{eff}\,(v_{i,j} + v_{j,i})\,]_{,j} + f_{bi} \qquad \text{(A-2)}$$

$$\rho\, v_j K_{,j} = \left(\frac{\mu_{eff}}{\sigma_k} K_{,j}\right)_{,j} + \rho\, G_K - \rho\, \varepsilon \qquad \text{(A-3)}$$

$$\rho\, v_j \varepsilon_{,j} = \left(\frac{\mu_{eff}}{\sigma_\varepsilon} \varepsilon_{,j}\right)_{,j} + \frac{\varepsilon}{K} \rho\,(C_1 G_K - C_2 \varepsilon) \qquad \text{(A-4)}$$

where $\mu_{eff} = \mu + \mu_t$ $\quad \mu_t = C_\mu \rho \dfrac{K^2}{\varepsilon}$ $\quad G_K = (v_{i,j} + v_{j,i})\, v_{i,j}$

$C_1 = 1.44$ $\quad C_2 = 1.92$ $\quad C_\mu = 0.09$ $\quad \sigma_k = 1.0$ $\quad \sigma_\varepsilon = 1.3$

Wall Function Approximations

for $y_+ > 11.5$

$$\tau_w = v_m \left(\rho \; K^{1/2} \; c_\mu \; \kappa \; \frac{1}{\ln(Ey_+)} \right) \tag{A-5}$$

$$K = (c_\mu)^{-1/2} \frac{\kappa^2 \, v_m^2}{\ln(Ey_+)} \tag{A-6}$$

$$\varepsilon = (c_\mu)^{3/4} \; K^{3/2} \; \frac{\ln(Ey_+)}{\kappa y_n} \tag{A-7}$$

for $y_+ \leq 11.5$

$$\tau_w = (c_\mu)^{1/2} \rho \, K \tag{A-8}$$

$$K = (c_\mu)^{-1/2} \left(\frac{v_m^2}{y_+^2} \right) \tag{A-9}$$

$$\varepsilon = (c_\mu)^{1/2} \; K \; \frac{v_m}{y_n} \tag{A-10}$$

where $y_+ = (c_\mu)^{1/4} \; \frac{\rho \, y_n}{\mu} \; K^{1/2}$, $\kappa = 0.4$, $E = 8.8$,

y_n is the normal distance of the near-wall grid node from the wall.